Sputtering Studies of Multi-Component Materials by Weight Loss and Cavity Ring-Down Spectroscopy

Azer P. Yalin[1], Vijaya Surla[2], Casey Farnell[3], Mark Butweiller[4], and John D. Williams[5]
Colorado State University, Fort Collins, Colorado, 80523

[Abstract] We report sputtering studies of multi-component spacecraft materials. We employ two complementary diagnostic methods: weight loss measurements and cavity ring-down spectroscopy (CRDS). The weight loss measurements provide total sputter yields as a function of ion energy and incidence angle. We present sputter yields from weight loss measurements for xenon ion sputtering of molybdenum, quartz, boron nitride, and kapton. The CRDS provides species-specific sputtering data (number density and velocity) as well as information on the differential (angular) sputtering distributions. We present CRDS results for the sputtering of molybdenum (from a molybdenum sample), and demonstrate measurements of multi-component materials by measuring the sputtering of chromium, iron, and molybdenum from inconel 718.

Nomenclature

$A(\nu)$	=	Absorption lineshape
A_{ki}	=	Einstein A coefficient, 1/s
Abs_{Eff}	=	Effective absorbance
a	=	Parameter determining shape of differential sputter yield
c	=	Speed of light, 2.998 x 10^8 m/s
E_b	=	Binding energy of target atoms, eV
g_i	=	Degeneracy of state i
j_i	=	Ion current density, mA/cm^2
j_t	=	Total current density (ions and fast neutrals), mAeq/cm^2
k	=	Boltzmann's constant JK^{-1}
$k(\nu)$	=	Absorption coefficient, m^{-1}
$k_{eff}(\nu)$	=	Effective absorption coefficient, m^{-1}
$L(\nu)$	=	Laser lineshape, Hz^{-1}
l	=	Length of the ring-down cavity, m
M	=	Molar mass, g
n	=	Number density, cm^{-3}
n_i	=	Number density of state i, cm^{-3}
P	=	Pressure, torr
$S(t, \nu)$	=	Ring-down signal
T	=	Chamber wall temperature, K
T_B	=	Boltzmann temperature, K
V	=	Velocity of sputtered particles, m/s
V_b	=	Velocity corresponding to binding energy, m/s
X	=	Position along optical axis, cm

[1] Assistant Professor, Mechanical Engineering, Colorado State University, and AIAA Member.
[2] Research Associate, Mechanical Engineering, Colorado State University, and AIAA Member.
[3] Research Associate, Mechanical Engineering, Colorado State University.
[4] Research Associate, Mechanical Engineering, Colorado State University.
[5] Assistant Professor, Mechanical Engineering, Colorado State University, and AIAA Member.

Y = Relative position of optical axis and target center-line, cm
$y(\alpha)$ = Differential sputter yield, atom/ion/sr
Z = Position (height) above target (along ion beam direction), cm
z = Position along ion beam, cm
α = Polar angle (relative to surface normal) for sputtered particles
λ_{CEX+sc} = Mean free path due to charge exchange and scattering, cm
λ_{CEX} = Mean free path due to charge exchange, cm
λ_{sc} = Effective mean free path due to scattering, cm
ν = Laser frequency, Hz
ν_{ki} = Transition frequency, Hz
σ_{CEX} = Cross-section for charge exchange, cm^2
τ = Ring-down time, s
τ_0 = Empty cavity ring-down time, s

I. Introduction

ELECTRIC propulsion (EP) technology is of importance for satellite re-positioning, station keeping, orbit transfer, and possibly collision avoidance maneuvering. A primary engineering challenge for Hall and ion thrusters is the need to flight-qualify them for use on spacecraft, which can involve operation for tens of thousands of hours. The lifetime of state-of-the-art Hall and ion thrusters is largely limited by sputter erosion of grids, electrodes, insulators, guard-rings and other components. (Sputtering is the process in which an energetic bombarding particle, usually an ion accelerated by an electric field, is incident on a material and causes the ejection of atoms, ions, and/or molecules from a surface.) For example, Fig. 1 shows a photograph of a sputter eroded accelerator grid from an NSTAR ion thruster after it was operated for 30 khrs. Sputtering processes also plays a key role in spacecraft contamination, since the sputtered particles can redeposit on other spacecraft surfaces.

In principle, both contamination and lifetime studies could be addressed by real-time tests; however, in practice, such approaches are prohibitive. Direct-duration life testing is no longer feasible for many reasons. First, the required time duration (in some cases five years or more) is long and the cost (~$1M per year or more) is high. Second, the long duration tests do not yield information on the causes of wear or about techniques to extend life. Further, such tests typically employ a restricted range of operating parameters, so that it is very difficult to determine how engine life depends on parameter settings. The long duration of tests required for qualification also limits the technology insertion schedule. The limitations in contamination studies are essentially analogous. Thus, in the absence of direct experimental testing, numerical modeling is typically employed to assess lifetime and contamination issues. However, such models require fundamental sputtering data, which is often not available. The focus of this work is to present methods for obtaining the fundamental sputtering data required for modeling of both erosion and spacecraft contamination. We are particularly interested in the sputtering of multi-component spacecraft materials, which in many cases has not been studied.

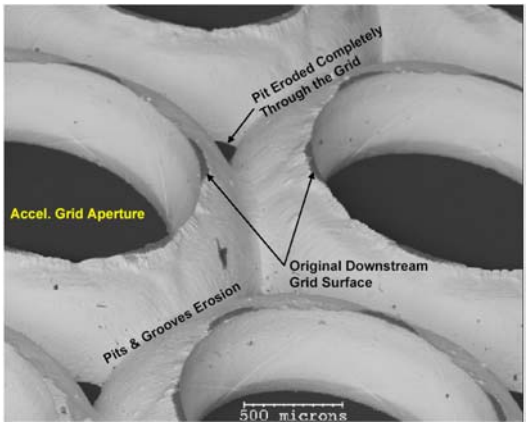

Figure 1. Accelerator grid from the NSTAR ELT thruster showing significant sputter erosion. The sputtered material can be re-deposited onto sensitive spacecraft surfaces causing contamination.

While (total) sputter yields for many single-component materials are well known (at least for energies well above the threshold), the sputter yields for many multi-component materials, of interest for spacecraft applications, are not known. Further, owing to the relative complexity of these materials and the sputtering processes, it is generally difficult to compute (*a priori*) their sputtering properties. In this work, we employ two complementary techniques to obtain sputter erosion data for several spacecraft materials. We employ a weight loss measurement method to measure the total sputter yields of the materials. The total sputter yields are needed to model (predict) component lifetimes. The total yields are determined from the change in sample mass for a known ion (and energetic neutral) dose. The weight loss measurements readily allow variation of the ion incidence angle. Using the weight loss technique, we study the sputtering of quartz, inconel, BN, and kapton by xenon at a range of ion energies and incidence angles. While the weight loss approach is useful for providing total sputter yields, it has no species specificity (meaning it can't resolve the sputtering of different species from multi-component materials), nor does it provide information on the ejection direction (differential yield) of the sputtered particles. Knowledge of the species-specific properties, and the angular properties, is needed to model (predict) contamination and re-deposition effects. To this end, we employ the cavity ring-down spectroscopy (CRDS) technique, which is an ultra-sensitive laser-based absorption method. In this work, we summarize the use of CRDS for sputter measurements, and we demonstrate its suitability for species-specific measurements from multi-component materials by measuring the sputtering of iron, molybdenum, and chromium from an inconel sample. In addition to measuring the sputtering number densities, we show that the CRDS technique allows measurement of the velocities and angular emission profiles (differential sputter yields) of the sputtered particles. The weight loss work is presented in Section II, while the CRDS work is presented in Section III. Conclusions are given in Section IV.

II. Weight Loss Measurements

A. Experimental

The sputter yield tests via weight loss measurements are carried out in a SPECTOR ion beam system (Ion Tech, Inc.). The 1000-liter SPECTOR chamber uses a CTI-400 cryogenic pump, and is equipped with a 16-cm diameter ion source. To ensure an accurate assessment of the sputtering behavior, a thorough characterization of the ion beam current density profile was conducted at four axial locations between the ion source exit plane and the plane where the samples were located. The ion current density profiles were integrated to determine the total ion current that passes each axial plane, and these values were plotted as a function of axial position to determine the effects of scattering and charge exchange. This was done to allow a calculation of the total flux of fast particles (ions and neutrals) that impinge upon the samples, since both ions and fast neutral particles cause sputtering.

A button probe enclosed within a Faraday cage was used to perform the current density measurements and is shown in Fig. 2. A flat nickel screen was placed in front of the button probe that was 75% transparent. A -30 V bias was applied to the Faraday cage structure and nickel mesh and a +30 V bias was applied to the button probe to ensure that only the current density of energetic beam ions was measured and that secondary electrons were returned to the probe surface and not allowed to perturb the measurement. The bias scheme chosen also minimizes the collection of low energy charge exchange ions present in the beam plasma that would similarly perturb the current density measurement.

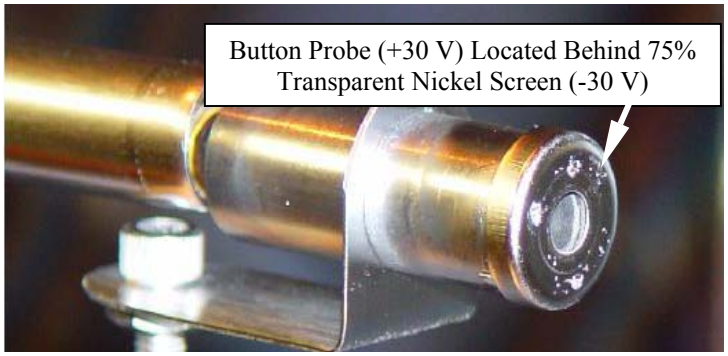

Figure 2. Probe used to measure ion current density profiles.

The probe was scanned perpendicularly across the axis of the ion beam at four different positions downstream of the ion source (at axial distances of 4.3 cm, 11 cm, 24 cm, and 38 cm). A typical ion current density profile obtained at 4.3 cm downstream of the ion source is shown in Fig. 3. For this measurement, the ion beam current and energy were set to 250 mA (± 10 mA) and 250 eV (± 15 eV), respectively. The ion beam current calculated by integrating the current density profile in Fig. 3 was 237 mA. The same beam sampled at 38 cm downstream of the ion source (at the target plane) yielded an integrated ion beam current measurement of 139.5 mA. The current density profile measured at 38 cm is shown in Fig. 4. The integrated beam current is plotted versus axial position in Fig. 5.

For computation of the dose of incident sputtering particles, we need to consider both incident ions as well as incident fast neutrals created from charge exchange (CEX) collisions. Here, we describe how we determine this combined current (or flux) from the measured ion current. The measured reduction in ion current versus axial position is due to both charge exchange collisions and scattering losses, and can be used to estimate the mean free path due to both charge exchange (CEX) and scattering collisions, λ_{CEX+sc}. We fit the ion current data in Fig. 5 with an exponential function and identify the 1/*e* length of the exponential fit as λ_{CEX+sc}. In this case we find $\lambda_{CEX+sc} = 70.4$ cm.

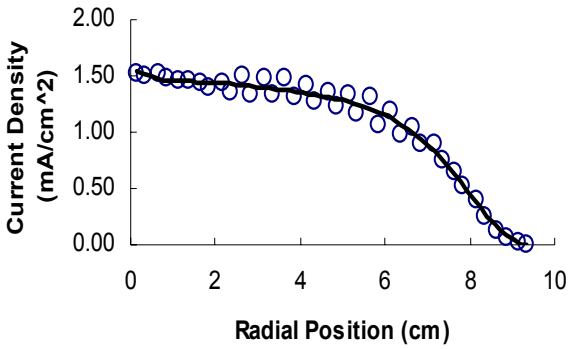

Figure 3. Current density profile measured 4.32 cm downstream of the ion source. The integrated beam current was 237 mA.

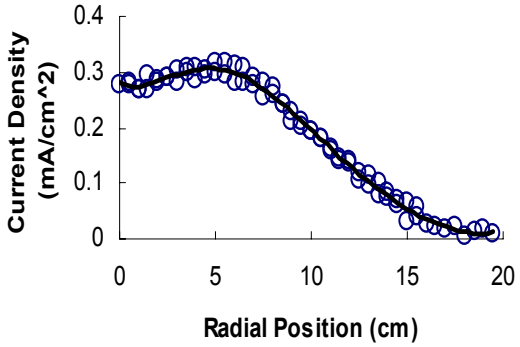

Figure 4. Current density profile measured at the target plane 38.0 cm downstream of the ion source. The integrated measured beam current was 140 mA.

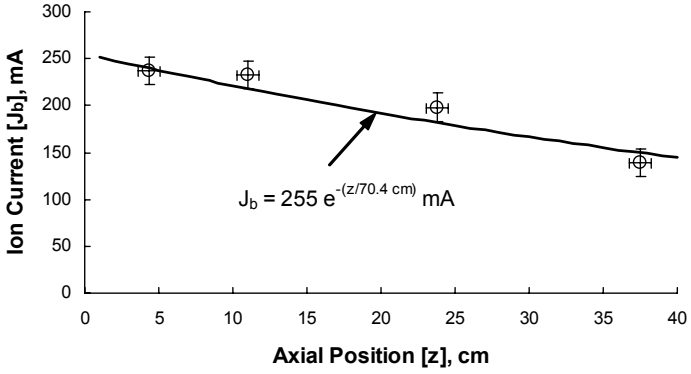

Figure 5. Integrated ion current behavior as a function of axial position for a 250 eV ion beam. Exponential curve fit to data yields a mean free path of 70.4 cm due to CEX and scattering collisions.

We can compute the CEX mean free path as:

$$\lambda_{CEX} = \frac{1}{n\sigma_{CEX}} \tag{1}$$

where σ_{CEX} represents the CEX cross-section (= $55\text{x}10^{-16}$ cm^2) for 250 eV xenon ions flowing through a background gas of neutral xenon atoms at a density, n, of

$$n = \frac{P}{kT} = 1.8\text{x}10^{12}\ \text{cm}^{-3} \tag{2}$$

where P represents the vacuum chamber pressure (which was measured to be $7.7\text{x}10^{-3}$ Pa), k is Boltzman's constant, and T the chamber wall temperature (measured as 303 K). The attenuation of the ion current due to CEX reactions follows a similar exponential trend, but with a mean-free path of λ_{CEX}=102 cm. The factor that the ion current density, j_i, (measured at the target location) must be multiplied by to determine the total flux of fast particles (i.e. ions and fast neutrals), j_t, in units of mAeq/cm^2 is $e^{38\text{-cm}/102\text{-cm}} = 1.45$. (Alternatively one can determine the effective mean free path for scattering, λ_{sc}, from the equation $1/\lambda_{CEX+sc}=1/\lambda_{sc}+1/\lambda_{CEX}$ as λ_{sc}=227 cm, and find the flux of fast particles from $j_{fast}=j_0\exp(-z/\lambda_{sc})$.) The radial distribution of total current density at the target plane, as well as the measured ion current density (from Fig. 4), is shown in Fig. 6. At the target plane (z = 38 cm), the measured (integrated) ion current was 140 mA (see Fig. 4), yielding a total fast particle current of 203 mA, the difference of 62 mA represents the fast neutral equivalent current. The equivalent current loss between source and target due to the scattering of ions and fast neutrals was estimated to be ~52 mA, i.e., 255 mA – 203 mA, (or $255\text{-}255\exp(-38/\lambda_{sc})$, with discrepancy from 52 mA due to difference of data and fit in Fig.5).

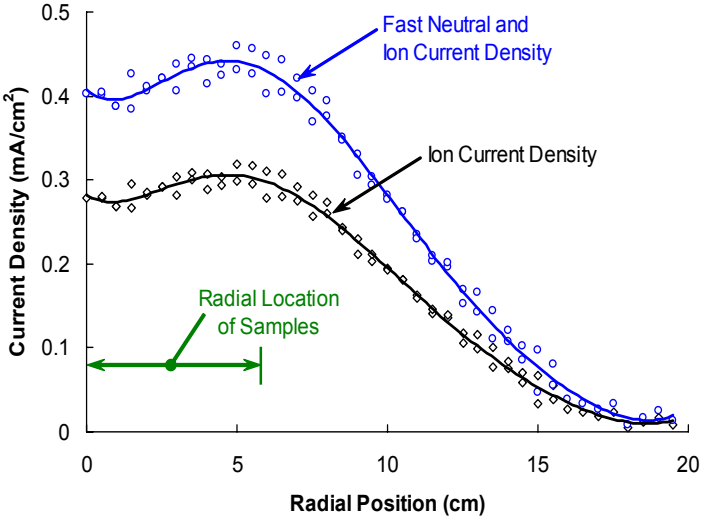

Figure 6. Total fast particle current density at the target plane. Note that the objects sputtered during these tests were placed at radial locations between 0 cm and 6 cm.

Samples used were typically 1-inch squares. The sample holders (holding 3 samples each) were machined of aluminum (6061). The holders were identical with square pockets that were 1.0" square. Graphite cover plates were then machined to serve as masks that were placed over the aluminum sample holders. Additionally, aluminum sidewall support structures and a 0˚, 30˚, 45˚, 60˚, 75˚ incident angle jig were machined to align and retain the sample holders at the proper orientation with respect to the ion beam. Finally, beam-defining slots were made of graphite to provide an initial masking of the ion beam and minimize the sputtering of sample holder mask hold-down screws. All machined parts were (1) placed in an ultra-sonic bath of cleaning solution/water to break down and remove the machining oils, then (2) cleaned with acetone, and finally (3) cleaned with methanol.

The samples were placed into the cleaned sample holders and affixed with masks. Then the holders were installed utilizing the alignment jig to ensure a proper angle of incidence with the ion beam. After assembling all of the sample holders on the sidewall structure, the apparatus was installed in the vacuum chamber and centered on the target using a laser alignment jig. Following alignment of the sample holder, the vacuum system was closed and pumped down to a pressure below $8x10^{-6}$ Torr. The quartz heaters installed within the SPECTOR vacuum facility were turned 'on' and the temperature of the sample holder was slowly raised to 150°C. The samples were baked for 10 hours. After which, they were pre-cleaned with a 250 eV, 250 mA argon ion beam for 1.5 hours. After pre-clean, the chamber was back-filled with nitrogen, and the samples were placed into an acrylic chamber that was positively pressurized with a constant purge of nitrogen.

A microgram scale was used to weigh the samples (before and after each sputtering session). Only one sample holder was removed from the apparatus at a time, keeping unmeasured samples in the N_2 environment. Each sample was weighed 5 times (obtaining an average) and returned to the nitrogen environment. The samples were then realigned with the incident angle alignment jig and placed inside the vacuum chamber on the cooling plate, where they were again aligned with the center of the beam and the system subsequently pumped down. A 100˚C, 1.5-hour bake-out was executed, and then the system was allowed to pump down to a chamber pressure below $1x10^{-7}$ Torr. The samples were then exposed to the xenon ion at prescribed test conditions for periods of several hours (depending on the expected erosion rate).

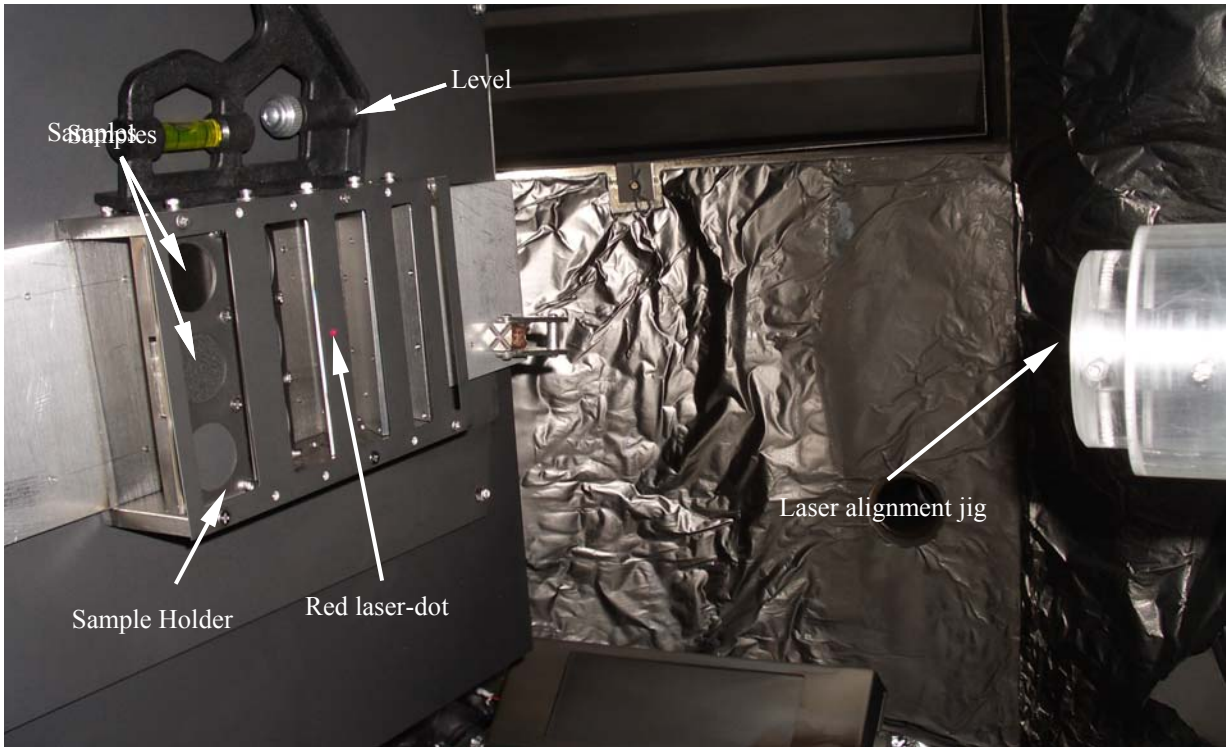

Figure 7. Samples and sample holder within SPECTOR ion beam system.

B. Measurement Results

In this section, sputter yield results are presented from molybdenum, quartz, kapton, and HBC grade boron nitride. Each of the materials was tested at incident ion angles of 0, 30, 45, 60, and 75 degrees for incident ion energies of 80, 150, 250, and 350 eV. The molybdenum was used as a control material to ensure that each test was comparable to the other tests and to allow for comparison to the quartz, kapton, and HBC grade boron nitride. Figure 8 shows a plot of sputter yield versus ion energy for xenon ions on molybdenum at normal incidence. The sputter yields in the current study (labeled "Weight Loss - Current Work") show reasonable comparison to previous tests at the same conditions.

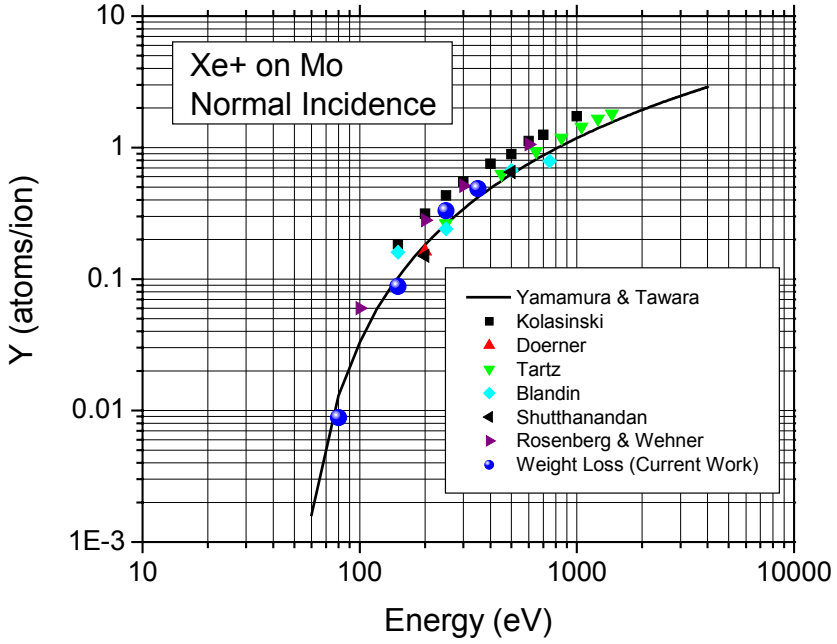

Figure 8. Comparison of molybdenum sputter yields for the current study versus previous results.

The sputter yield results are summarized in Table 1. The sputter yield data are presented in units of volume loss per equivalent coulomb delivered to the surface (mm^3/coul). These units allow the most direct comparison of volumetric erosion rates (for materials of different densities). The fourth column in the quartz, kapton, and boron nitride sections is the wear rate of the given material compared (normalized) to molybdenum (at the same incidence angle and ion energy). The volumetric sputter yield of each sample is found using Eqn. (1), where Δm represents the mass loss (caused during a 20+ hour ion beam exposure), ρ is the measured density of the sample, j_t is the total current density on the target (including both ions and fast particles), t is the exposure time, and $A\cos(\alpha)$ is the exposed area projected to the ion beam:

$$Yield = \frac{\Delta m}{\rho\, j_t\, t\, A\, \cos(\alpha)} \tag{3}$$

The data of Table 1 are plotted in Figures 9 though 12 as a function of ion energy (graphs labeled "a") and ion incidence angle (graphs labeled "b"). It was empirically determined that given the ~20 hour test time used in the experiment, the detection limit of the weight loss method was about 0.005 mg/Coulomb (at normal incidence). In some cases (i.e. for low energy sputtering of low sputter yield materials), the measured sputter yields fall below the detection limit and thus are not statistically significant (i.e. they are below the noise floor). To make this visually apparent, the detection limit is plotted as a hatched line in Figures 9b-12b. (Note that the detection limit is fundamentally in units of mass per coulomb, so that when we covert it to volume per coulomb, the numerical values vary for different materials.) In particular, the sputter yields for kapton and boron nitride samples, especially for the lower energies of 80 and 150 eV tend to be below the detection limit. For sputter yields below our detection limit, more sensitive measurement techniques (such as cavity ring-down spectroscopy) are required.

The trends apparent in Figures 9 though 12 are as expected: for a given material, the total sputter yields increases with energy, and for a given material and energy, the total sputter yield increases with incidence angle for small incidence angles, prior to reaching a maximum for an incidence angle in the vicinity of 45-60 degrees. Of the materials studied, quartz has the largest volumetric wear rate (which is above that for molybdenum), while the wear rates for kapton and HBC grade boron nitride are comparable to one another and less than molybdenum.

Table 1. Volumetric sputter yield for xenon on molybdenum, quartz, kapton, and HBC grade boron nitride.

Molybdenum Density = 10.22 (gm/cm^3)

Ion Incidence Angle (degrees)	Incident Ion Energy (eV)	Sputter Yield (mm^3/Coulomb)
0	80	0.0009
	150	0.0086
	250	0.0322
	350	0.0476
30	80	0.0016
	150	0.0227
	250	0.0611
	350	0.0857
45	80	0.0021
	150	0.0250
	250	0.0790
	350	0.1076
60	80	0.0022
	150	0.0188
	250	0.0715
	350	0.0995
75	80	0.0012
	150	0.0054
	250	0.0206
	350	0.0254

Quartz Measured Density = 2.05 (gm/cm^3)

Ion Incidence Angle (degrees)	Incident Ion Energy (eV)	Sputter Yield (mm^3/Coulomb)	Wear Rate (wrt Mo)
0	80	0.0052	6.10
	150	0.0259	3.02
	250	0.0460	1.43
	350	0.0645	1.36
30	80	0.0068	4.12
	150	0.0338	1.49
	250	0.0686	1.12
	350	0.0971	1.13
45	80	0.0087	4.10
	150	0.0493	1.97
	250	0.1136	1.44
	350	0.1670	1.55
60	80	0.0087	3.87
	150	0.0447	2.37
	250	0.1303	1.82
	350	0.2078	2.09
75	80	0.0080	6.68
	150	0.0281	5.24
	250	0.0731	3.56
	350	0.1372	5.40

Kapton Density = 1.42 (gm/cm3)

Ion Incidence Angle (degrees)	Incident Ion Energy (eV)	Sputter Yield (mm3/Coulomb)	Wear Rate (wrt Mo)
0	250	0.0101	0.31
	350	0.0189	0.40
30	250	0.0104	0.17
	350	0.0198	0.23
45	250	0.0116	0.15
	350	0.0242	0.22
60	250	0.0096	0.13
	350	0.0208	0.21
75	250	0.0078	0.38
	350	0.0177	0.70

HBC grade boron nitride Measured Density = 1.98 (gm/cm3)

Ion Incidence Angle (degrees)	Incident Ion Energy (eV)	Sputter Yield (mm3/Coulomb)	Wear Rate (wrt Mo)
0	250	0.0056	0.17
	350	0.0112	0.24
30	250	0.0075	0.12
	350	0.0160	0.19
45	250	0.0098	0.12
	350	0.0227	0.21
60	250	0.0133	0.19
	350	0.0305	0.31
75	250	0.0062	0.30
	350	0.0240	0.95

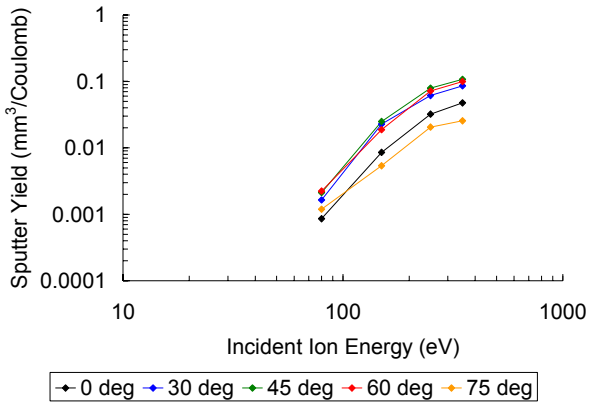

Figure 9a. Sputter yield of Molybdenum for incident ion energies of 80, 150, 250, and 350 eV.

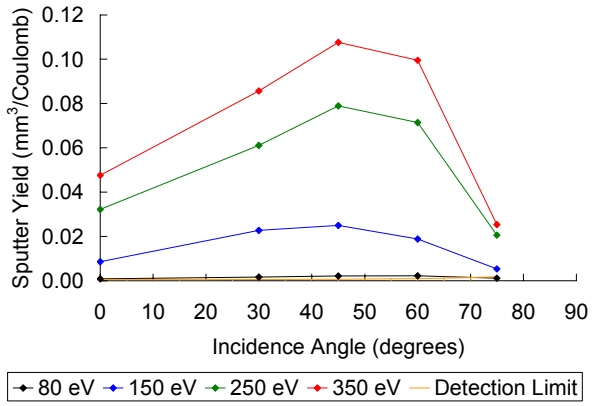

Figure 9b. Sputter yield of Molybdenum versus incidence angle for ion energies of 80, 150, 250, and 350 eV.

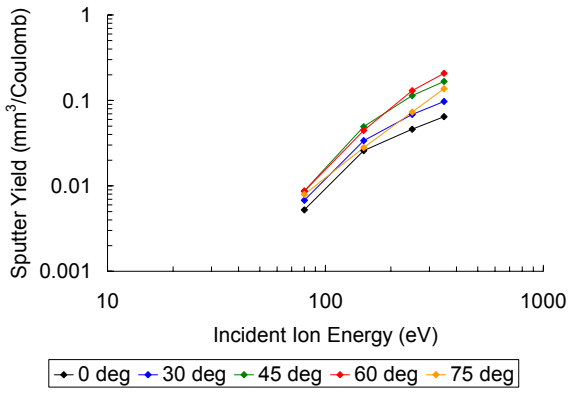

Figure 10a. Sputter yield of Quartz for incident ion energies of 80, 150, 250, and 350 eV.

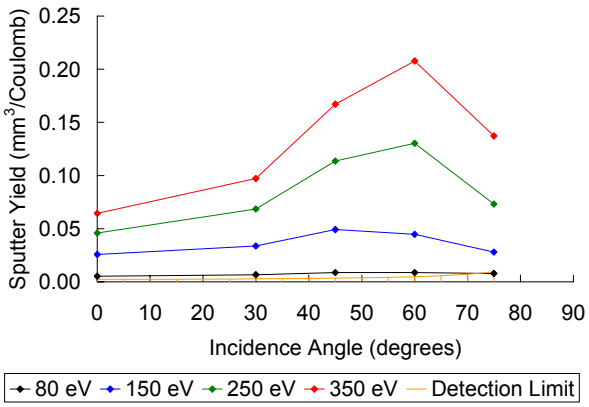

Figure 10b. Sputter yield of Quartz versus incidence angle for ion energies of 80, 150, 250, and 350 eV.

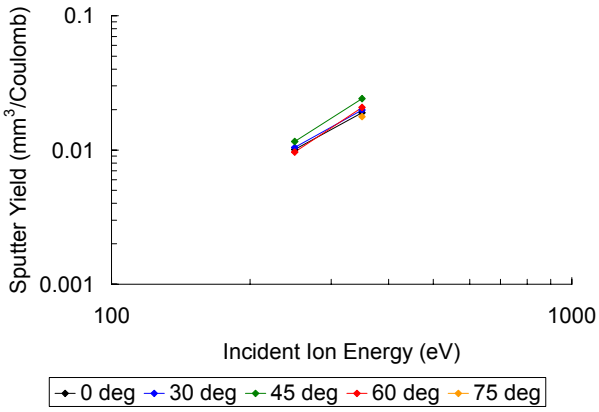

Figure 11a. Sputter yield of Kapton for incident ion energies of 250 and 350 eV. Data below detection limit are not plotted.

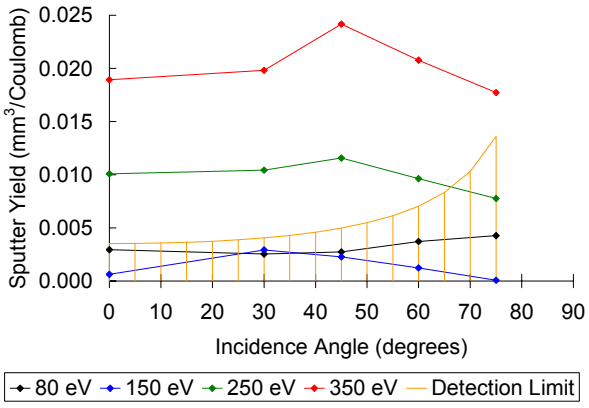

Figure 11b. Sputter yield of Kapton versus incidence angle for ion energies of 80, 150, 250, and 350 eV. Note that the sputter yields for the 80 and 150 eV ion energies fall below the detection limit.

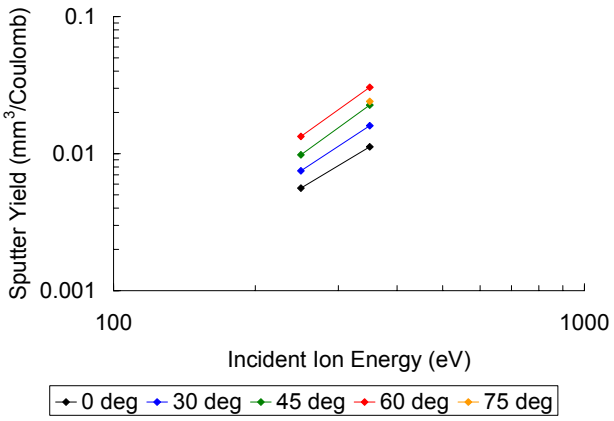

Figure 12a. Sputter yield of HBC grade boron nitride for incident ion energies of 250 and 350 eV. Data below detection limit are not plotted.

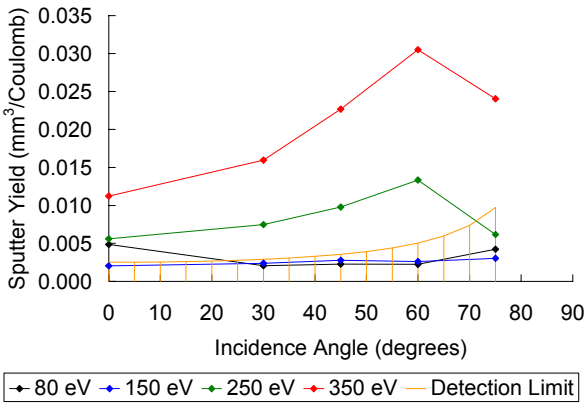

Figure 12b. Sputter yield of HBC grade boron nitride versus incidence angle for ion energies of 80, 150, 250, and 350 eV. Note that the sputter yields for the 80 and 150 eV ion energies fell below the detection limit.

III. Cavity Ring Down Spectroscopy

A. CRDS Experimental Set-Up and Approach

Cavity ring-down spectroscopy is a laser-based absorption method offering very high sensitivity. Detailed reviews[1,2] of the technique may be found in references. Our development of CRDS for sputter diagnostics has been previously described[3-5]. In CRDS, the absorbing sample is contained within a high-finesse optical cavity typically formed from two (or three) high-reflectivity mirrors. The laser beam is coupled into the cavity and passes back-and-forth many times within it. Upon each reflection at the rear cavity-mirror, a small fraction of the cavity light leaks out to a photodetector which measures the decay of light intensity within the optical cavity. With no absorber present (or the laser detuned from the absorption) the cavity decays primarily due to mirror reflective loss. When the laser light is resonant with a sample absorption line the decay is hastened. The change in decay rates may be found from the change in ring-down signals and related to the sample's absorbance (concentration). The technique affords high sensitivity owing to a combination of long effective path length and insensitivity to laser energy fluctuations. Under appropriate conditions, the ring-down signal $S(t, \nu)$ decays (single-) exponentially versus time as[6, 7]:

$$S(t,\nu) = S_0 \exp\left[-t/\tau(\nu)\right]$$

$$1/\tau(\nu) = \frac{c}{l}\left[\int k_{Eff}(x,\nu)dx + (1-R)\right] \quad ; \quad k_{Eff}(\nu) \equiv \int_{-\infty}^{+\infty} d\nu'\, L(\nu'-\nu)\, k(\nu') \tag{4}$$

where τ is the 1/e time of the decay (termed the ring-down time), c is the speed of light, l is the cavity length, $k_{eff}(\nu)$ is the effective absorption coefficient, ν is the laser frequency, 1-R is the effective mirror loss (including scattering and all cavity losses), and $L(\nu)$ is the laser lineshape function. (If the absorber is uniformly present over a column length l_{abs} then $\int k_{Eff}(x,\nu)dx$ can be replaced with the product of $k_{Eff}(\nu)l_{abs}$.) As in conventional absorption, the effective absorption coefficient accounts for line broadening arising from the laser lineshape. In practice, the measured ring-down signal is fitted with an exponential, and the ring-down time τ is extracted. Combining τ with the "empty cavity ring-down time", τ_0 (which in practice is measured by detuning the laser) allows determination of the (effective) sample absorbance, Abs_{Eff}, and (effective) absorption coefficient, k_{Eff}:

$$Abs_{Eff}(\nu) \equiv l_{abs}k_{Eff}(\nu) = \frac{l}{c}\left[\frac{1}{\tau(\nu)} - \frac{1}{\tau_0}\right] \tag{5}$$

As in conventional absorption, both the laser and absorber lineshapes are needed to determine the actual absorbance (and number density) if the effective absorbance is measured at a single wavelength. A more practical approach is to scan the laser frequency across the absorption line and to measure the frequency-integrated spectrum (i.e. the line area). Because the area of the effective absorbance spectrum is equivalent to the area of the (actual) absorbance spectrum, this method removes lineshape dependences. Assuming the absorption line parameters are known, the measured area $\int Abs_{Eff}(\nu)d\nu$ of a transition from a lower atomic state i to upper state k can be readily converted to the path-integrated concentration of the lower state n_i as:

$$\int n_i dx = 8\pi \frac{g_i}{g_k}\frac{\nu_{ki}^{\,2}}{A_{ki}c^2}\left(\int Abs_{Eff}(\nu)d\nu\right) \tag{6}$$

where g_i, g_k are the level degeneracies, ν_{ki} is the transition frequency, A_{ki} is the transition Einstein A coefficient, and c is the speed of light. The measured lower state population can be converted to overall species population through the energy level population distributions[3,4].

Figure 13 shows a schematic diagram of the bench-top sputtering apparatus consisting primarily of an ion beam and target, housed within a vacuum facility, and surrounded by a CRDS system. The CRDS set-up uses an optical parametric oscillator (OPO) laser system (doubled idler) with parameters: repetition rate = 10 Hz, pulse width ~ 7 ns, pulse energy (at the cavity input) ~ 100 μJ, and linewidth ~0.002 nm. We use a linear ring-down cavity of 75 cm length with 50 cm radius-of-curvature mirrors. Modeling results by Spuler et al.[8] indicate that this will be a near optimal cavity geometry in terms of spatial resolution (beam walk) and stability. In order to prevent possible saturation effects, the laser energy is reduced with an attenuator to ~100 μJ/pulse prior to cavity injection. The ring-down signal is collected behind the output mirror with a fast photomultiplier tube (Hamamatsu R3896). Ring-down signals are fit between 90%-10% of the peak amplitude. We use area (frequency-integrated) measurements of absorbance in our analyses. We use reduce temporal fitting windows to verify that our measurements are not affected by laser bandwidth effects[7] (to within the quoted error bars).

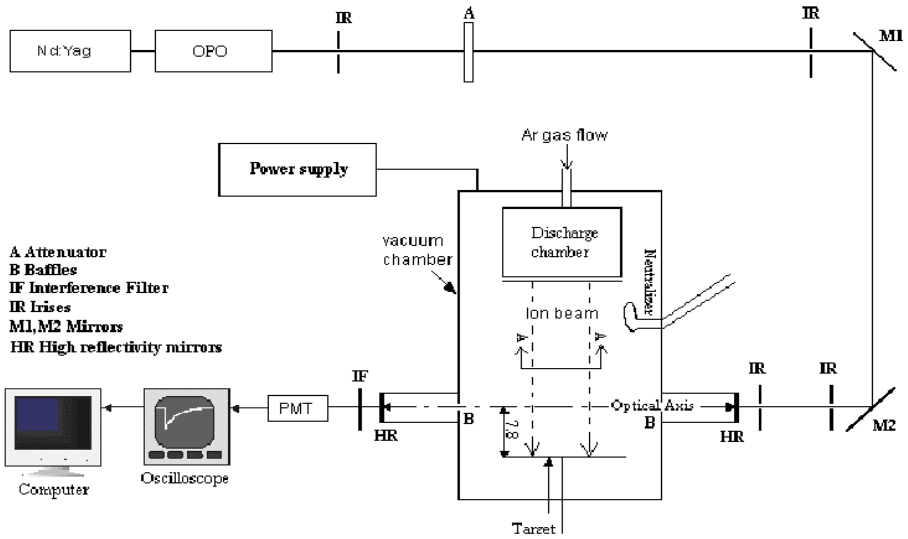

Figure 13. Schematic diagram of sputtering apparatus and CRDS system.

A roughing and turbo-pump are used to bring the pressure to approximately 10^{-6} torr under no-flow conditions. A small argon flow (1 sccm) is used to feed the system. The ion beam is extracted from an 8-cm diameter structurally integrated thruster and is nominally normally incident on the target (comprised of the material under investigation). The thruster operates with an IonTech power supply (MPS 3000), with typical beam currents and voltages of about 10-100 mA, and 400-1000 V respectively. The ion beam current density profiles are presented below with our analysis. Past research shows that sputter yields from metallic species (as well as the velocities of the sputtered particles) can be influenced by oxygen and other impurities. Because we operate at relatively high current densities (approximately 1 mA/cm^2), the flux of ions to the target is at least an order of magnitude higher than the flux of impurity particles, so that poisoning effects should be negligible[9].

We have recently added a spatial scanning capability in order to obtain angularly resolved sputtering information (i.e. a description of how much material is sputtered (or ejected) into given directions relative to the target's surface normal). As shown in Fig. 14, we scan a "strip" of target material laterally relative to the (fixed) optical axis. We define Y as the position of the target centerline relative to the optical axis. At each lateral position, Y, the CRDS detection system measures the path-integrated number density of sputtered particles along the optical axis (using Eq. (6)). The scanning approach allows us to obtain a "Spatial Profile" which is the dependence of the CRDS signal (path-integrated number density) on the lateral position Y. We employ a numerical model (using certain assumptions on the form of the differential sputter yield) to infer the differential sputter yield from the Spatial Profile. The differential sputter yield, y, describes the angular dependence of the sputtering. Note that the scanning-inversion approach presented here can only be used for differential sputter yields with no azimuthal dependence (i.e. the only angular dependence is on the polar angle α), which limits its use to normally incident ions or energetic ions for non-normal incidence. The ion beam is nominally uniform over the full extent of target displacements, though we correct our data to account for non-uniformity of the ion beam current density (which we have experimentally characterized).

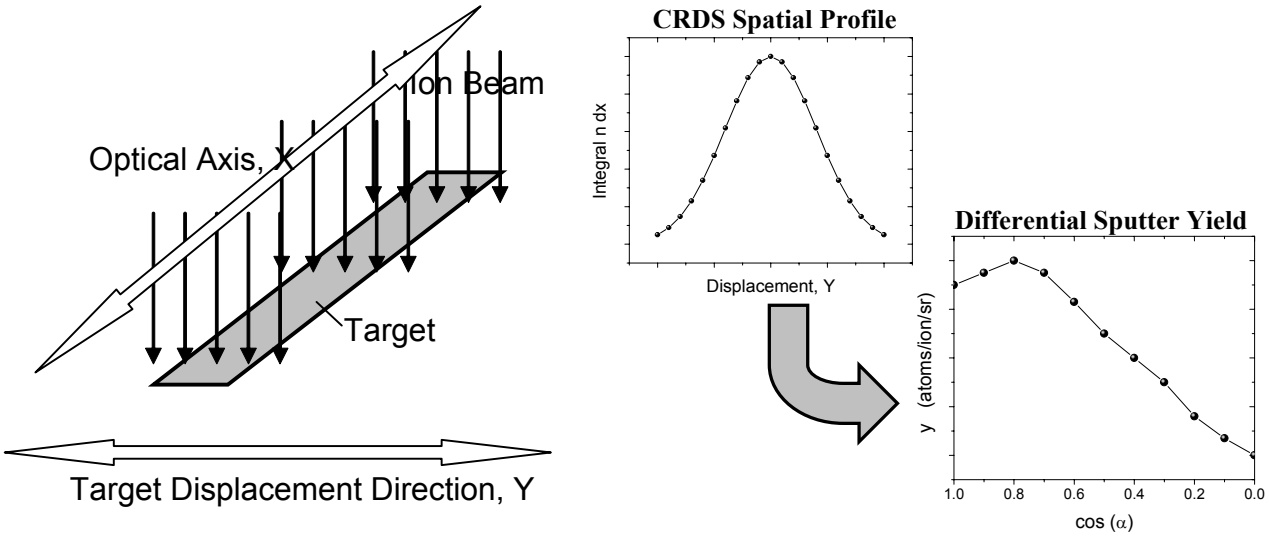

Figure 14. Left: Schematic of spatial scanning of target (*Y* direction). The CRDS Spatial Profile is obtained by measuring the CRDS signal (Integral n dx) at a series of lateral positions, *Y*, of the target relative to optical axis. Right: Schematic of inversion approach. The Differential Sputter Yield, *y*, is inferred from the CRDS Spatial Profile. The Differential Sputter Yield, *y*, describes the amount of sputtering as a function of ejection polar angle α.

B. Analysis – CRDS Finite Element Model

A finite element approach is used to model and analyze the CRDS sputtering signals (including determination of the angular shape of the differential sputter yield). Figure 15 schematically illustrates the finite element discretization of the target and optical axis.

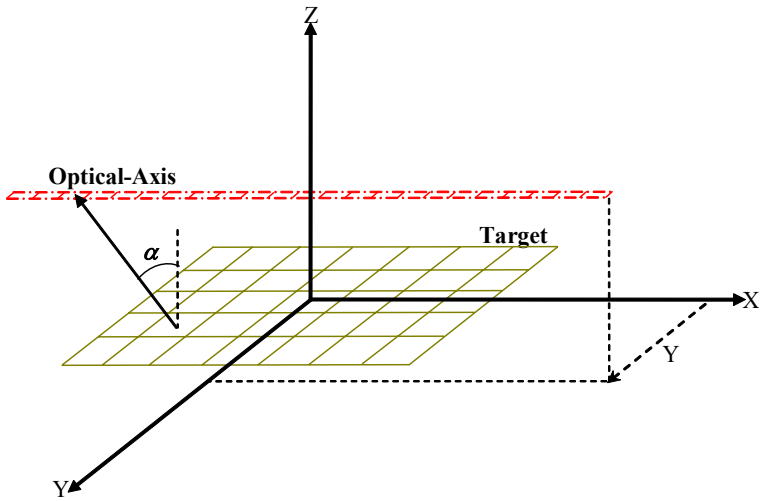

Figure 15. Schematic diagram of the finite element approach. The polar angle α is measured relative to the surface normal.

CRDS, like other laser absorption methods, is inherently a path-integrated ("line of sight") technique. For a given measurement (e.g. lateral position *Y* above the target), the absorption line area (from CRDS) is proportional to the path-integrated number density. A finite element approach is used to calculate the path-integrated number-density by integrating (summing) the number densities along the optical axis (and finding the number density at a given point along the optical axis by integrating (summing) the sputtering contributions from each point on the target):

$$\int n dx\Big|_y = \int_{beam}\left[\oiint_{target} n(r,\alpha)\,dA\right]dx = \int_{beam}\left[\oiint_{target}\left(\frac{y(\alpha)I}{r^2}\left\langle\frac{1}{\mathrm{v}(\alpha)}\right\rangle\right)dA\right]dx \tag{7}$$

Figure 16 shows the approach used to determine the number density contribution, $n(r,\alpha)$, at a location along the beam due to sputtering from a target element. (Note that we require the number density at the location, not the total number of atoms in a volume.) The number density contribution depends on the differential sputter yield in the given direction $y(\alpha)$, the radial separation between the target element and beam element r, the current (particles per unit time) incident on the target I, and the average of the inverse of the ejection velocity $\langle 1/V \rangle$. The current on the target element is found from an experimentally measured current profile, while the other quantities are functions of the polar angle α and radius r (which are in turn computed from the relative locations of the target element and beam element). The differential sputter yield, current density, and ejection velocity are discussed below.

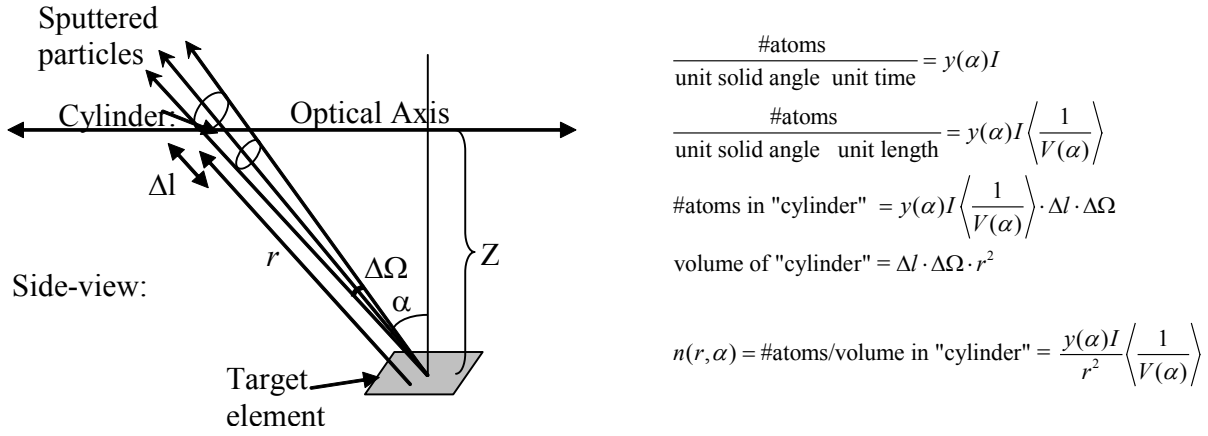

Figure 16. Calculation of number density of sputtered particles, $n(r,\alpha)$, at some location along the optical axis due to sputtering from a target element. r is the radial distance from target element to location along optical axis, and α is the corresponding polar angle (measured relative to surface normal).

The current incident on a target element is found from the product of the area of the target element (typically about 1 mm x 1 mm) and the current density incident at that location. We have experimentally characterized the current density of our source. Figure 17 shows an example of a measured current density profile, and a polynomial fit to the profile (used in our calculations) for a plane that is 3 cm above the target (Z=3cm), for beam current of 30 mA and beam voltage of 750 V.

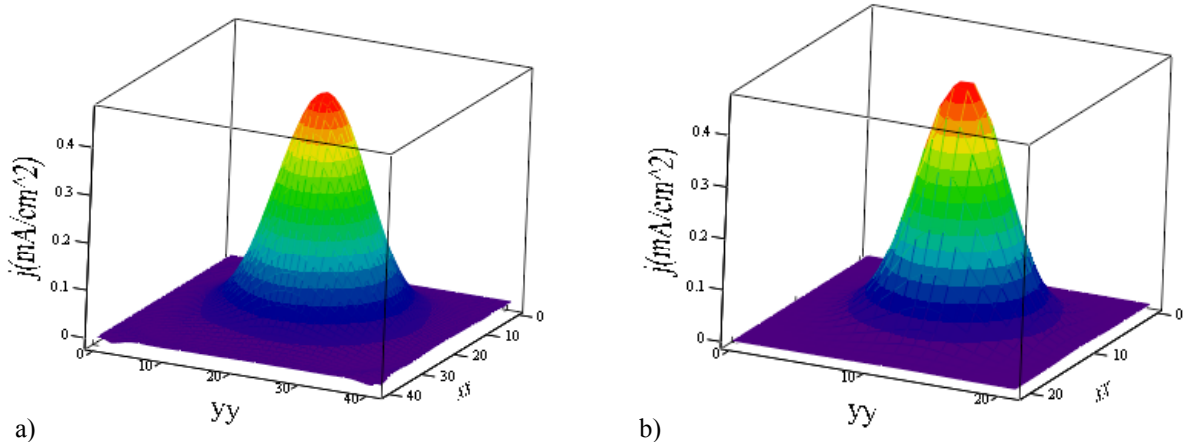

Figure 17. Current density profiles at Z=3cm for beam current of 30 mA and beam voltage of 750 V. a) Measured profile. b) Polynomial fit to profile.

We assume that the (flux) distribution of the velocity profile of ejected particles, $f(V)$, does not vary with polar angle. We adopt a Thompson distribution for the flux distribution of ejected velocities[10]:

$$f(V) \propto \frac{V^3}{\left(V^2 + V_b^2\right)^{n+1}}; \quad V_b = \sqrt{\frac{2E_b}{M}} \tag{8}$$

where E_b is the binding energy, M is the molar mass of the target material, and we (generally) take the exponent n as 1.54[11]. From this distribution we compute the average value of inverse velocity, $\langle 1/V \rangle$, required for the computation on Eq. (7). Recent modeling shows that there may be some dependence of the distributions on ejection angle[11], and we are currently investigating these effects.

The formalism presented above allows us to compute the (path-integrated) CRDS signals, and their dependence on the lateral position Y, for given differential sputter yield profiles. Our approach is to infer the experimental angular sputtering profile by comparing the measured data (spatial profile) with a series of simulated profiles (and identifying the best match). Note that the *total* sputter yield is treated independently, and here we are concerned only with the *angular shape* of the differential sputter yield. As mentioned, we treat the case where the angular shape varies with only the polar angle (no azimuthal variation). To encompass the range of possible profiles, we parameterize with a single parameter 'a' allowing a range of profile shapes between under-cosine ($a>0$) and over-cosine ($a<0$)[12]:

$$y(\alpha) = \frac{Y}{\pi}\cos(\alpha)\left(1 + a\left(1 - 2\cos^2(\alpha)\right)\right) \tag{9}$$

Figure 18 shows plots of the shapes of the differential sputter (angular) profiles as a function of polar angle (α) for several values of parameter a (for a total sputter yield Y=1).

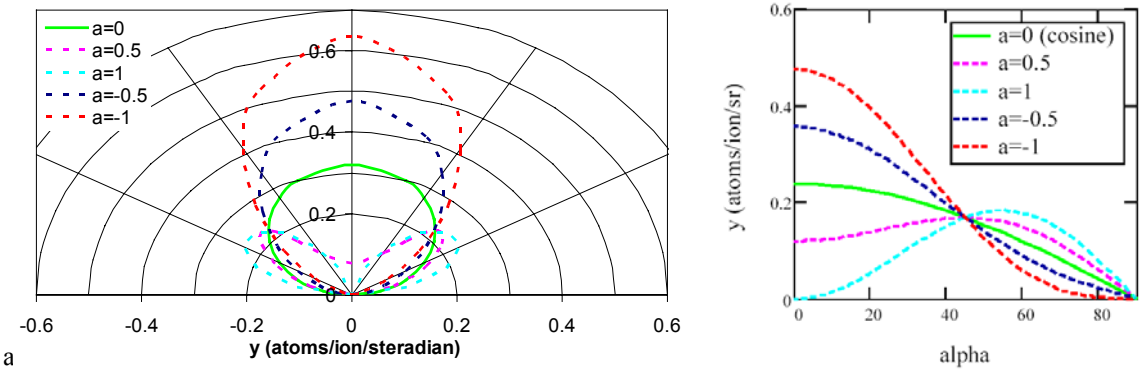

Figure 18. Differential sputter yield profile shapes for different values of parameter *a*. a) Polar plot. b) Standard plot. *a*=0 corresponds to a diffuse (cosine) profile, while *a*<0 yields over-cosine profiles, and *a*>0 yields under-cosine profiles

Figure 19 shows examples of simulations of spatial scanning profiles (path integrated concentration at different lateral positions) for several sputter profile shapes (i.e. several values of the parameter a). The simulations use the experimentally measured current profile shown in Fig. 17, a molybdenum target (E_b=6.82 eV) of 8 cm x 2 cm (with the 8 cm parallel to optical axis), total sputter yield Y = 0.9 atoms/ion, and the optical axis at a height of Z=3 cm above the target plane. Essentially, for larger values of the a parameter the angular sputtering is increasingly under-cosine (wider), so that a larger proportion of the material is ejected away from surface normal and the spatial profiles of Fig. 19 become broader. By matching the experimentally measured spatial profiles to the modeled curves one can infer the shape (a parameter) of the sputtering profile. (The left/right asymmetry in the modeled curves is due to slight asymmetry in the current density profile of the ion beam.)

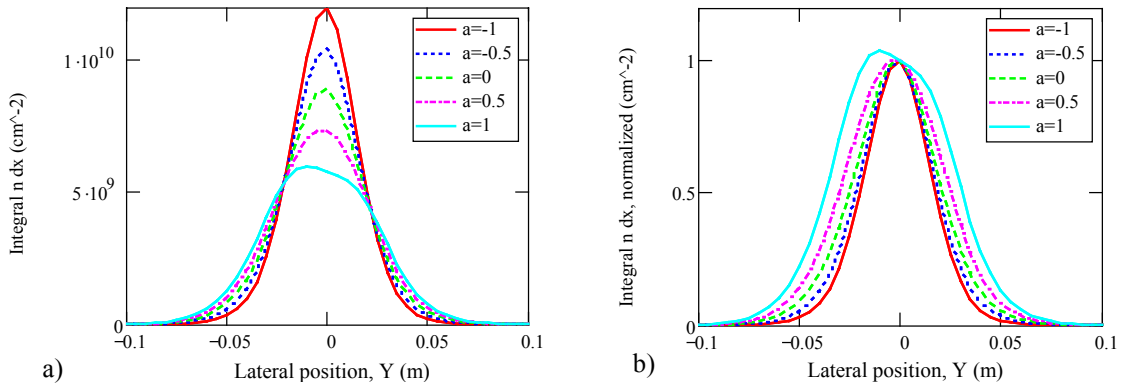

Figure 19. CRDS spatial profiles. a) CRDS signal versus lateral (scan) position *Y*. The curves are for different angular sputter yield profiles (*a* parameters). b) As left, but normalized to give unity at *Y* = 0.

C. Species Measurements from Single-Component Materials

Section D contains sputtering results of several constituents (chromium, iron, and molybdenum) from an inconel alloy sample. Here, we show measurements of a single component-material by presenting results of molybdenum sputtering measurements (from a molybdenum sample).

Panel A) of Fig. 20 shows a partial energy level diagram for molybdenum including all energy levels below 1 eV. The electronic ground state of atomic Mo has only one level (no fine-structure splitting). After the ground state, the next lowest energy level is at 1.33 eV so that to a good approximation all population can be expected to reside in the ground state[4]. We show three absorption lines in the energy level diagram. Since all the population is in a single state, probing any of these lines is sufficient to determine the Mo number density.

Panel B) of Fig. 20 shows the (sputtered) Mo number density versus beam current at a height of Z=7.8 cm above a 15 cm diameter target, for sputtering by an argon ion beam of energy 750 eV. The inset shows absorbance spectra from two of the aforementioned lines for one value of beam current (18 mA). The area(s) of the measured line(s) yield the path-integrated number density. The number densities displayed assume (for simplicity in this case) a uniform concentration of Mo over the target length of 8 cm. As expected, we observe a linear dependence of number density on current passing through the origin.

For more quantitative validation we use our finite-element model to compare measured and modeled values of path-integrated concentration. Note that although we can generally apply this model for single-component materials, we often cannot do so for multi-component materials since the (total and differential) sputter yields and ejection velocities may not be known. Relative to our past work[3,4], we have advanced the sputter model to include the experimentally measured current density profile. As an example of comparison between model and experiment, for ion beam conditions of 30 mA, and 750 eV, and a target of length 8 cm (aligned with the beam) by 2 cm, at a height 2 cm above the beam (centered in the Y direction), the measured path integrated number density is 1.5 ± 0.1 x 10^{10} cm^{-2} while the modeled value (assuming a sputter yield of 0.9 from Yamamura et al.[14], and a diffuse differential sputtering profile (a=-0.2 ± 0.2) is 1.51±0.08 x 10^{10} cm^{-2}. The good agreement between measurement and model provides quantitative validation of our technique.

The spatial-scanning approach for determination of angularly resolved (differential) sputter yield is demonstrated in Panel C) of Fig. 20. Experimental conditions are as specified in the preceding paragraph. The plot shows the (normalized) path-integrated concentration (found from the CRDS lineshape areas) versus lateral position Y (see Figs. 14, 15). Experimental points are shown as symbols, while modeled profiles (curves) are shown for different values of the a parameter (i.e. different differential sputter yield profiles). We find the best agreement between experiment and model for an a parameter of a=-0.2±0.2, corresponding to an approximately diffuse sputter (but slightly over-cosine) profile. (We have performed analogous measurements at a height of Z=3 cm above the target and find the same result.) Past work at CSU using a quartz crystal microbalance (QCM) setup has found a profile with a=0.2 (slightly under-cosine) for these conditions, and the modest discrepancy with the CRDS results is being investigated. Note that owing to the path-integrated nature of CRDS (and the modeling required), the CRDS technique does not provide as direct a measurement of the differential sputter yield profile as does the QCM method[15]; however, the CRDS has the advantages of allowing species-specific measurements and providing higher sensitivity.

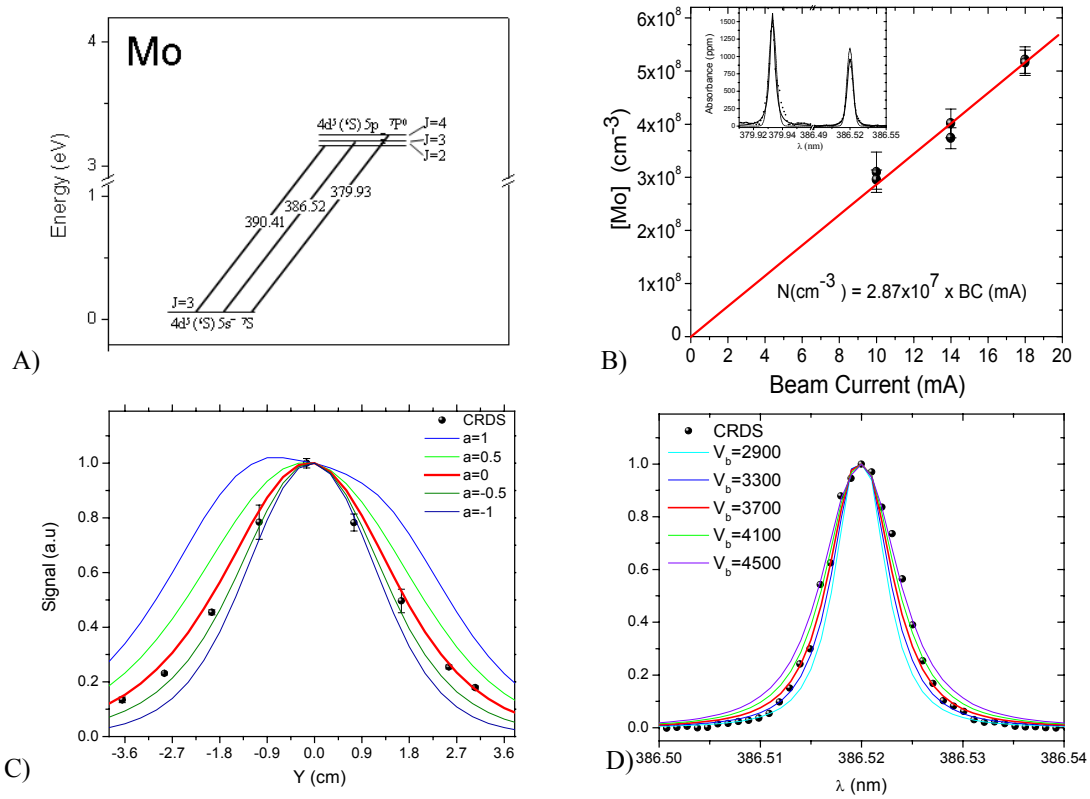

Figure 20. A) Partial energy level diagrams for Mo with all energy levels below 1 eV included, wavelengths given as vacuum, and all parameters (energy configurations, terms, *J* values, and wavelength) from NIST. B) Mo number density versus beam current (see text). Inset show absorption spectra measured at 18 mA. C) Normalized CRDS signals (path-integrated Mo concentration) versus lateral position *Y* demonstrating use of spatial-scan approach to infer the shape (*a* parameter) of the differential sputter yield profile (see text). D) Velocity measurement using CRDS.

Panel D) shows velocity measurements from the spectral lineshapes[5]. Briefly, we model the spectral lineshape based on Doppler shifts corresponding to Thompson velocity distributions (eqn. (8)) with n=1.54 (not Maxwell-Boltzmann distributions). For this case (conditions as above), we find the best agreement between model and experiment for a characteristic velocity of V_b=3700 ± 400 m/s, which is in good agreement with the expected value of V_b=3700 m/s (based on the binding energy).

D. Species Measurements from Multi-Component Materials

In this section we present (the first) demonstrative CRDS measurements of multi-component materials. We measure the sputtering of chromium, iron, and molybdenum from inconel 718. The major constituents of inconel 718 (by mass) are: Ni+Co~50-55%, Cr~17-21%, Fe~11-24%, Mo~3%, Cb+Ta~5%. We could readily measure Cr, Fe, and Mo (and other species may also be possible). From the measured spectra we determine number densities, velocities, and shapes of the sputtering profiles using analogous methods to those presented for pure Mo sputtering (Section III.C above). We analyze the spatial profiles and resulting angular sputtering distributions of the sputtering species and compare with sputtered Mo from the (pure) molybdenum target. We also examine the species-specific sputter yields and species fluxes versus inconel composition.

For all the CRDS measurements in this section, the experimental conditions are: 750 eV Ar^+ beam striking an inconel target of 8 cm (in the beam direction) by 4 cm, with the optical axis at a height Z=2 cm above the target. The target was sputter cleaned by Ar^+ ions prior to the measurements. For Mo, we use the same detection scheme as was presented in Section III.C. Our work on detection of iron with CRDS has been previously reported[4]. Iron has 5 fine-structure levels (J=0,1,2,3,4) within its ground electronic state. Here, we measure populations only of the

lowest of these levels (J=4) using the absorption line at 386.1 nm. Following our earlier work (and assuming the same population distribution[4]) we convert the population of this measured state to the overall iron population. Cr has only one energy level in the ground state (no fine splitting structure) with its next lowest energy level at 0.94 eV. For typical population distributions of sputtered particles, this means that >~98% of the overall population resides in the ground state (as we assume here) though we have not made a detailed study of the Cr level populations.

First we present results of differential sputter yield measurements by the spatial scanning technique outlined above (and used for pure Mo sputtering). Figure 21 shows the normalized CRDS signals (path-integrated concentrations) versus position Y for Mo, Fe, and Cr (symbols), as well as modeled curves for different values of the a parameter (i.e. different shapes of the differential sputter yield profiles). Again, we assume that the ejection velocity (V_b) flux distributions do not change with ejection angle so that the *normalized* profiles do not change for the different species (even though their total sputter yields and ejection velocity magnitudes do vary). Again, we assume a value of n=1.54 for the Thompson distributions (Eq. (5)). For both iron and molybdenum we find a best fit between experiment and model for a parameter of a = 0.3 ± 0.2, corresponding to under-cosine profiles. Note that for sputtering of Mo from a pure Mo sample, we found a = -0.2 ± 0.2, indicating that the angular profile of the sputtering for Mo from inconel is angularly broader (more under-cosine) as compared to the sputtering of Mo from a pure molybdenum sample. In the multi-component samples, the presence of other species influences the sputtering characteristics. For sputtering of chromium atoms sputtered from inconel target, the best fit is a = -0.2±0.2 indication that the chromium is ejected with a narrower (more over-cosine) angular profile than the molybdenum and iron.

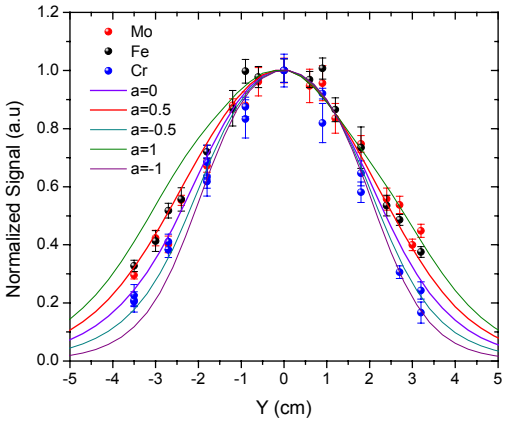

Figure 21. Spatial profiles of sputtered Mo, Fe and Cr from inconel.

Using the species-specific angular profiles (values of a parameter) found above we use our lineshape model to determine the species-specific velocities. Knowing the velocities and angular profiles, we can use our finite element model to determine species-specific (total) sputter yields from measured path-integrated concentrations. Table 2 presents initial results of such measurements at the conditions given earlier. For comparison, we also use the TRIM simulation model[16] (in which we input the composition of our multi-component sample) to predict sputter yields using the binding energies found from the CRDS velocity measurements. We find good agreement between the measured and TRIM sputter yield values (though we recognize the potential limitations of using the TRIM model for multi-component samples in this energy range). We also examine the fluxes of the different species being sputtered off the target. The experimentally measured species fluxes are proportional to the experimentally determined total yields (since the total yield multiplied by the total current gives the flux). At steady-state conditions, the relative fluxes of particles leaving the surface should match the target composition[17]. In the table we show the experimentally measured species fluxes as well as the target's species composition (both normalized by chromium) and find good agreement between the sets of values.

Table 2. Summary of species-specific sputter yields and fluxes for sputtering of Mo, Fe and Cr from inconel.

$Metal_i$	CRDS: $Yield_i$	TRIM: $Yield_i$	CRDS: $Flux_i$ / $Flux_{Cr}$	Target Composition: $Fraction_i$ / $Fraction_{Cr}$
Mo	0.038±0.008	0.036±0.006	0.12±0.03	0.086±0.016
Fe	0.280±0.05	0.320±0.18	0.90±0.25	0.87±0.47
Cr	0.310±0.06	0.310±0.20	1	1

IV. Conclusions

We report sputtering studies of multi-component spacecraft materials by weight-loss as well as by cavity ring-down spectroscopy (CRDS). The weight loss measurements are used to measure (total) sputter yields of molybdenum, quartz, boron nitride, and kapton as a function of ion energy (80, 150, 250, and 350 eV) and incidence angle (0, 30, 45, 60, 75 degrees). For measurement validation, we compare the sputter yields for molybdenum found in this study to those from other researchers and find good agreement. The data for other species are consistent with expected trends. We find that quartz has a higher volumetric sputter yield than molybdenum, while the kapton and boron nitride have lower values. Empirically, we find that for ~20-hour measurement durations, our weight loss measurements have a detection limit of about 0.005 mg/Coulomb (at normal incidence). For lower sputtering one must either perform longer tests or use a more sensitive method (such as CRDS).

We also report CRDS sputtering measurements. We describe the finite element model used to describe the sputtering signals as well as an approach to infer the shape of the angular (differential) sputter yield profiles by scanning the target relative to the optical axis. For sputtering of molybdenum (from a pure molybdenum target) we present measurements of number density, velocity, model validation, and profile shape. We also present the first species-specific CRDS measurements of multi-component materials. We use CRDS to detect sputtered chromium, iron, and molybdenum from an inconel 718 sample. We find that the angular profiles for molybdenum and iron are similar to one another and slightly under-cosine (which is broader than was found for the sputtering of molybdenum from a pure molybdenum sample at the same ion energy), while the chromium is ejected with a narrower (more over-cosine) angular profile. The measured species-specific sputter yields are in good agreement with those predicted by TRIM simulation and the measured species-specific sputtered fluxes are consistent with the expected values based on the target composition.

Acknowledgments

The financial support provided by the Air Force Research Labs, Edwards Air Force Base is greatly appreciated.

References

[1]Busch, K.W., and Busch, M.A., "Cavity-Ringdown Spectroscopy," ACS Symposium Series, Vol. 720, 1999.

[2]Berden, G., Peeters, R., and G. Meijer, "Cavity Ring-Down Spectroscopy: Experimental Schemes and Applications," International Reviews in Physical Chemistry, Vol.19, No.4, p. 565-607, 2000.

[3]Surla, V., Wilbur, P.J., Johnson, M., Williams, J.D., Yalin, A.P., "Sputter erosion measurements of titanium and molybdenum by cavity ring-down spectroscopy," Review of Scientific Instruments, Vol.75, No.9, p. 3025-3030, 2004.

[4]Yalin, A.P., Surla, V., Butweiller, M., Williams, J.D., "Detection of Sputtered Metals using Cavity Ring-Down Spectroscopy," Applied Optics, Vol.44, No.30, p. 6496-6505, 2005.

[5]Yalin, A.P., Surla, V., "Velocity Measurements by Cavity Ring-Down Spectroscopy," Optics Letters, Vol.30, No.23, p.3219-3221, 2005.

[6]Zalicki, P. and Zare, R.N., "Cavity ring-down spectroscopy for quantitative absorption measurements," Journal of Chemical Physics, Vol. 102, No.7, p. 2708-17, 1995.

[7]Yalin, A.P., and Zare, R.N., "Effect of Laser Lineshape on the Quantitative Analysis of Cavity Ring-Down Signals," Laser Physics, Vol.12, No.8, p. 1065-1072, 2002.

[8]Spuler, S. and Linne, M., "Numerical analysis of beam propagation in pulsed cavity ring-down spectroscopy," Applied Optics, Vol.41, No.15, p. 2858-2868, 2002.

[9]Pellin, M.J., Young, C.E., Mendelsohn, M.H., Gruen, D.M. , Wright, R.B., and Dewald, A.B., "Oxygen and titanium sputtering yields as determined by laser fluorescence and auger electron spectroscopy for monolayer oxygen coverage of polycrystalline Ti," Journal of Nuclear Materials, 111 & 112, p. 738-743, 1982.

[10]Pellin, M.J., R.B. Wright, and D.M. Gruen, "Laser fluorescence spectroscopy of sputtered zirconium atoms," Journal of Chemical Physics, Vol.74, No.11, p. 6448-6457, 1981.

[11]Stepanova, M., Dew, S.K.," Anisotropic energies of sputtered atoms under oblique ion incidence," Nuc. Inst. Meth. B. , Vol. 215, No. 3-4, p. 357-365, 2004.

[12]Jones Jr., R.E., "Theories of Distribution of Deposit from Sputtered Disk and Rectangular Electrodes," I.B.M. Journal of Research and Development, p. 27-34, 1972.

[13]Yalin, A.P., Surla, V., "Determination of Number Density and Velocity of Sputtered Particles by Cavity Ring-Down Spectroscopy," Paper No. IEPC- 2005-300, in 29th International Electric Propulsion Conference, Princeton, NJ, 2005.

[14]Yamamura, Y. and Tawara, H., "Energy Dependence of Ion-Induced Sputtering Yields from Monatomic Solids at Normal Incidence," Atomic Data and Nuclear Data Tables, Vol.62, No.2, p. 149-253, 1996.
[15]Yalin, A.P., Williams, J.D., Surla, V., Wolf, J., Zoerb, K.A., "Azimuthal Differential Sputter Yields of Molybdenum by Low Energy Xe^+ Bombardment," AIAA JPC, Sacramento, CA, 2006.
[16]TRIM, software available from URL: http://www.srim.org/
[17]Smentkowski, "Trends in Sputtering," Progress in Surface Science, Vol.64, p. 1-58, 2000.